



# Carbon-enhanced electrodeposited SnO<sub>2</sub>/carbon nanofiber composites as anode for lithium-ion batteries



Mahmut Dirican<sup>a,b</sup>, Meltem Yanilmaz<sup>a</sup>, Kun Fu<sup>a</sup>, Yao Lu<sup>a</sup>, Huseyin Kizil<sup>b</sup>,  
Xiangwu Zhang<sup>a,\*</sup>

<sup>a</sup> Fiber and Polymer Science Program, Department of Textile Engineering, Chemistry and Science, North Carolina State University, Raleigh, NC 27695-8301, USA

<sup>b</sup> Nano-Science and Nano-Engineering Program, Graduate School of Science, Engineering and Technology, Istanbul Technical University, Istanbul 34469, Turkey

## HIGHLIGHTS

- SnO<sub>2</sub>-electrodeposited porous and nonporous CNFs anodes are introduced.
- Loading of electrodeposited SnO<sub>2</sub> nanoparticles was increased by using porous CNFs.
- SnO<sub>2</sub>-electrodeposited nanofibers were coated with amorphous carbon by CVD method.
- CVD carbon coating led to high capacity retention and coulombic efficiency.

## ARTICLE INFO

### Article history:

Received 24 February 2014

Received in revised form

1 April 2014

Accepted 17 April 2014

Available online 30 April 2014

### Keywords:

Lithium-ion battery

Carbon nanofibers

Tin oxide

Chemical vapor deposition

Capacity retention

Coulombic efficiency

## ABSTRACT

Tin oxides (SnO<sub>2</sub>) are promising anode material candidate for next-generation lithium-ion batteries due to their high capacity, low cost, high abundance, and low toxicity. However, the practical use of SnO<sub>2</sub> anodes is currently limited by their large volume changes during cycling. Severe volume changes of SnO<sub>2</sub> anodes lead to intense pulverization and loss of electrical contact between the active material and carbon conductor. Herein, we introduce binder-free SnO<sub>2</sub>-electrodeposited carbon nanofibers (CNF@SnO<sub>2</sub>) and SnO<sub>2</sub>-electrodeposited porous carbon nanofibers (PCNF@SnO<sub>2</sub>) composites that can maintain their structural stability during repeated charge–discharge cycling. Results indicated that the amount of the electrodeposited SnO<sub>2</sub> nanoparticles and the capacity of the resultant composites were successfully enhanced by using a porous nanofiber structure. Both CNF@SnO<sub>2</sub> and PCNF@SnO<sub>2</sub> composites were also coated with amorphous carbon layers by chemical vapor deposition to further improve the structural stability. Electrochemical performance results demonstrated that the combination of porous nanofiber structure and CVD amorphous coating led to a novel carbon-coated PCNF@SnO<sub>2</sub> composite anode with high capacity retention of 78% and large coulombic efficiency of 99.8% at the 100th cycle.

© 2014 Elsevier B.V. All rights reserved.

## 1. Introduction

Among the various existing rechargeable battery technologies, rechargeable lithium-ion batteries are considered as the most preferred rechargeable batteries in recent years because of their superior properties such as high energy density, long cycle life and good power performance [1,2]. Development of high-capacity electrode materials for lithium-ion batteries is crucial for

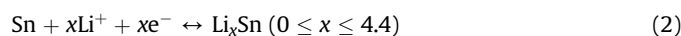
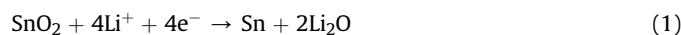
technological improvements on grid storage, mobile electronic devices and electric vehicle technologies using lithium-ion batteries as the power source [3–6]. Current commercial lithium-ion batteries use graphitic materials in the anode. However, the theoretical capacity (372 mAh g<sup>−1</sup>) of graphitic anode materials cannot meet the ever-growing capacity requirements of future portable electronics and electric vehicle technologies [7,8].

Lithium storage capacities of alloy-type anodes (e.g., silicon, tin, germanium, and their oxides) are much higher than that of currently-used intercalation-type graphite anode. Among different alloy-type anodes, tin oxides (SnO<sub>x</sub>,  $x = 1$  and 2) are considered as one of the most promising candidates for next-generation lithium-ion batteries because of their high capacity, low cost, high

\* Corresponding author. Tel.: +1 919 515 6547; fax: +1919 515 6532.

E-mail addresses: [xiangwu\\_zhang@ncsu.edu](mailto:xiangwu_zhang@ncsu.edu), [xwzhang01@yahoo.com](mailto:xwzhang01@yahoo.com) (X. Zhang).

abundance, and low toxicity [9,10]. For SnO<sub>2</sub> based anodes, two principle electrochemical reactions occur during charge–discharge cycling:



The first reaction leads to the reduction of SnO<sub>2</sub> to Sn and is irreversible. Formation of a solid electrolyte interface (SEI) at low voltage with this first reaction brings together apparent capacity decrease of the electrode during the initial cycles. In contrast, the second reaction is reversible. During insertion and extraction processes, lithium ions are repeatedly stored and released by the formation of alloyed Li<sub>x</sub>Sn and de-alloyed Sn, respectively [11,12]. For the second reaction, the theoretical capacity is reported as 790 mAh g<sup>−1</sup>, which is more than twice the theoretical capacity of graphite. However, similar to other alloy-type anode materials, insertion of lithium ions into the Sn structure during the second reaction causes high volumetric change (up to 300%), which results in intense pulverization and loss of electrical contact between the active material and carbon conductor [13–15]. Aforementioned drawbacks cause severe capacity fading of SnO<sub>2</sub> based anodes during lithium insertion and extraction processes. Reducing the size of SnO<sub>2</sub> particles into the nanoscale range and dispersing them into carbon structures are proven to be two effective methods for addressing the volumetric change problem of SnO<sub>2</sub> based anodes. Although using the nanoscaled SnO<sub>2</sub> can reduce the pulverization associated with the volumetric change, the cycling performance is still unsatisfactory because of the severe aggregation of nanoscale SnO<sub>2</sub> particles during the lithiation and de-lithiation processes [16,17]. Dispersing SnO<sub>2</sub> nanoparticles into carbon structures leads to improved cycling performance [18]. Various carbon nanostructures, such as graphene, mesoporous carbon materials, graphite, carbon nanotubes, and carbon nanofibers, etc., have been extensively studied as host materials for SnO<sub>2</sub>/carbon composite anodes [3,19–21]. In SnO<sub>2</sub>/carbon nanocomposite anodes, the carbon matrix serves as a physical buffer to accommodate the volume change of the active material (i.e., cushion effect) during cycling [22,23]. Nevertheless, carbon has limited lithium storage capacity, leading to reduced ultimate capacity for most SnO<sub>2</sub>/carbon nanocomposite anodes [12,15,24].

Recently, SnO<sub>2</sub> nanoparticle-loaded electrospun carbon nanofiber (CNF) composites have been introduced as high-capacity anode materials for lithium-ion batteries. Integration of the SnO<sub>2</sub> nanoparticles with CNFs can be achieved by the electrodeposition of SnO<sub>2</sub> nanoparticles directly onto electrospun CNFs [21,25]. Electrodeposition is a widely-used technique to modify the properties of carbon nanomaterials and it enables the synthesis of metal oxide particles on one-dimensional carbon surfaces [26,27]. Compared to other surface coating techniques, such as physical vapor deposition, atomic layer deposition, etc., the electrodeposition method is considered to be a feasible, scalable, cost-effective, low-temperature, and controllable processing approach. Electrodeposited CNF@SnO<sub>2</sub> composites were previously introduced as binder-free anodes for lithium-ion batteries [25]. However, two main drawbacks have been observed for previously reported electrodeposited CNF@SnO<sub>2</sub> composite anodes: limited SnO<sub>2</sub> nanoparticle loading and unstable SEI formation on the anode surface. The loading amount of electrodeposited SnO<sub>2</sub> nanoparticles can be enhanced by increasing the surface area of CNFs while stable SEI formation on the anode surface can be achieved by additional nanoscale carbon coating. This leads to novel carbon-coated SnO<sub>2</sub>-electrodeposited nonporous and porous carbon nanofibers (PCNFs) for use as high-capacity anodes for Li-ion batteries. Fabrication

procedures are schematically presented in Fig. 1. Electrospun CNFs and PCNFs were first oxidized to create surface functional groups to serve as defect sites during electrodeposition. SnO<sub>2</sub> nanoparticles were then electrodeposited onto the oxidized nanofibers to obtain CNF@SnO<sub>2</sub> and PCNF@SnO<sub>2</sub> composites. In order to further improve the cycling performance, these nanofiber composites were further coated with nanoscale carbon layers by chemical vapor deposition (CVD) method to form carbon-coated nanofibers, i.e., CNF@SnO<sub>2</sub>@C and PCNF@SnO<sub>2</sub>@C composites. Electrochemical performance results show that among all nanofiber composites studied, PCNF@SnO<sub>2</sub>@C composite has the highest capacity retention of 78% and largest coulombic efficiency of 99.8% even after 100 cycles.

## 2. Experimental

### 2.1. Chemicals and reagents

Polyacrylonitrile (PAN, Pfaltz & Bauer Inc., 150,000 g mol<sup>−1</sup>), polymethyl methacrylate (PMMA, Aldrich), *N,N*-dimethylformamide (DMF, Aldrich), tin (II) chloride (SnCl<sub>2</sub>, Aldrich), and sulfuric acid (H<sub>2</sub>SO<sub>4</sub>, Aldrich) were used without further purification. Deionized water was used throughout the electrodeposition experiments.

### 2.2. Electrospinning and carbonization of nonporous carbon nanofibers

PAN (8 wt%) was dissolved in DMF and mechanically stirred at 60 °C for 24 h. The as-prepared PAN/DMF solution was then electrospun into nanofibers with a flow rate of 0.75 ml h<sup>−1</sup>, a voltage of 16 kV, and a tip-to-collector distance of 20 cm. Electrospun PAN nanofibers were stabilized in air environment at 280 °C for 5.5 h with a heating rate of 5 °C min<sup>−1</sup> and then carbonized at 700 °C for 2 h in argon atmosphere with a heating rate of 2 °C min<sup>−1</sup>, during which PAN was pyrolyzed to carbon. The resultant CNFs were used as the working electrode in the electrodeposition of SnO<sub>2</sub> nanoparticles.

### 2.3. Electrospinning and carbonization of porous carbon nanofibers

A DMF solution of 8 wt% PAN and PMMA blend (PAN-to-PMMA mass ratio = 9/1) was prepared at 60 °C under mechanical stirring for 24 h. The as-prepared PAN/PMMA/DMF solution was then electrospun into nanofibers with a flow rate of 0.75 ml h<sup>−1</sup>, a voltage of 16 kV, and a tip-to-collector distance of 20 cm. Electrospun PAN/PMMA nanofibers were stabilized in air environment at 280 °C for 5.5 h with a heating rate of 5 °C min<sup>−1</sup> and then carbonized at 700 °C for 2 h in argon atmosphere with a heating rate of 2 °C min<sup>−1</sup>, during which PAN was pyrolyzed to carbon and PMMA was thermally degraded to create a porous structure in the carbon matrix. As-prepared PCNFs were used as the working electrode in the electrodeposition of SnO<sub>2</sub> nanoparticles.

### 2.4. Electrodeposition and CVD coating of nonporous and porous carbon nanofibers

For the electrodeposition process, a three-electrode cell, which composed of a working electrode (CNFs or PCNFs), a counter electrode (Pt wire), and a reference electrode (Ag/AgCl/4.0 M KCl), was used. Prior to electrodeposition, CNFs and PCNFs were oxidized in a 1 M H<sub>2</sub>SO<sub>4</sub> solution by cyclic voltammetry between −0.7 and 1.2 V at a scan rate of 50 mV s<sup>−1</sup> for 100 cycles. Electrodeposition of SnO<sub>2</sub> nanoparticles on oxidized CNFs and PCNFs was performed on an AQ4 Gamry Reference 600 electrochemical workstation at room temperature by applying a potential of −0.2 V vs. Ag/AgCl/4.0 M KCl

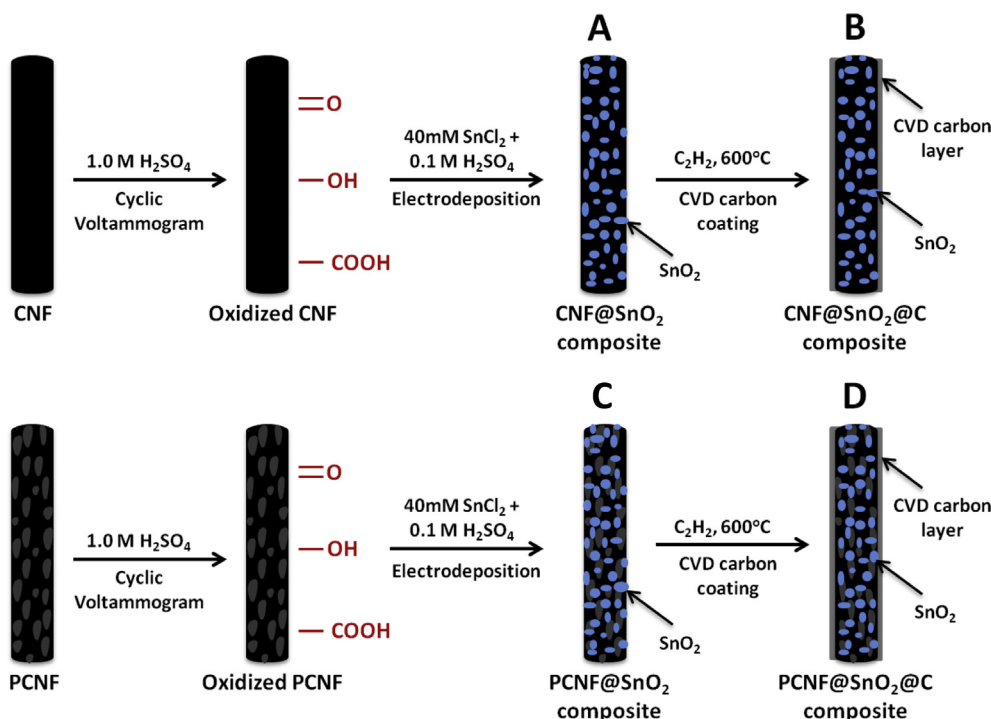


**Fig. 1.** Schematic illustration of the fabrication processes of (A) CNF@SnO<sub>2</sub>, (B) CNF@SnO<sub>2</sub>@C, (C) PCNF@SnO<sub>2</sub>, and (D) PCNF@SnO<sub>2</sub>@C composites.

in a 0.04 M SnCl<sub>2</sub> + 0.1 M H<sub>2</sub>SO<sub>4</sub> solution for 20 h. Electrodeposited nanofibers were calcinated at 600 °C for 1 h in argon atmosphere to obtain CNF@SnO<sub>2</sub> and PCNF@SnO<sub>2</sub> composites. Electrodeposition experiments were conducted three times for each sample to ensure the reproducibility of the process.

CVD amorphous carbon coating was carried out to obtain CNF@SnO<sub>2</sub>@C and PCNF@SnO<sub>2</sub>@C composites by using acetylene (C<sub>2</sub>H<sub>2</sub>) as the carbon precursor gas. Carbon coating of CNF@SnO<sub>2</sub> and PCNF@SnO<sub>2</sub> composites was accomplished in a horizontal CVD tube furnace (inner tube diameter: around 6.8 cm). The CVD coating process occurred at 600 °C for 1 h with 600 sccm flow rate of acetylene while the system was set to 20 torr.

### 2.5. Structure characterization

The morphology of composite nanofibers was examined by field emission scanning electron microscope (FE-SEM, JEOL 6400F) and transmission electron microscope (TEM, JEOL JEM-2000FX). The structure of composite nanofibers was investigated by Fourier transform infrared spectroscopy (FTIR, Nicolet Nexus 470), wide angle X-ray diffraction (WAXD, Rigaku Smartlab), and a Renishaw Raman microscope (514 nm).

### 2.6. Electrochemical evaluation

The electrochemical properties of composite nanofibers were tested using CR 2032-type coin cells. These composite nanofibers formed free-standing, conductive nonwoven mats that were used directly as the working electrode without adding polymer binder or conductive agent. Lithium ribbon (99.9%, Aldrich) was used as the counter electrode and Celgard 2400 membrane was used as the separator. The electrolyte consisted of a 1 M solution of LiPF<sub>6</sub> dissolved in 1/1 (V/V) ethylene carbonate (EC)/ethylmethyl carbonate (EMC). Coin cells were assembled in a high-purity argon-filled glove box. The electrochemical performance was investigated by

carrying out galvanostatic charge–discharge experiments at constant current density of 100 mA g<sup>−1</sup> (around C/10) with cut-off potentials of 0.01 and 2.00 V using LAND-CT 2001A battery test system. The rate performance was measured using the same instrument at current densities of 100 mA g<sup>−1</sup>, 200 mA g<sup>−1</sup>, 400 mA g<sup>−1</sup>, and 800 mA g<sup>−1</sup>.

The overall reproducibility of the testing results was assessed by conducting all measurements on at least twenty samples for each composite.

## 3. Results and discussion

### 3.1. Morphology and structure

As illustrated in Fig. 1, prior to the electrodeposition process, negatively charged functional groups such as quinoid (=O), hydroxyl (−OH) and carboxyl (−COOH) were created on the surfaces of electrospun CNFs and PCNFs with the oxidation treatment step. These surface functional groups provided defect sites for the deposition of SnO<sub>2</sub> nanoparticles [28]. During the electrodeposition, the SO<sub>4</sub><sup>2−</sup> ions in the acidic solution were electrochemically reduced on the surfaces of CNFs or PCNFs, leading to the formation of OH<sup>−</sup> ions. Further reaction of tin (II) with OH<sup>−</sup> ions on the fiber surfaces resulted in the formation of SnO<sub>2</sub> nanoparticles. As-prepared CNF@SnO<sub>2</sub> and PCNF@SnO<sub>2</sub> composites were then coated with nanoscale amorphous carbon layers by the CVD method.

Fig. 2 shows the FTIR spectra of CNFs and oxidized CNFs, which confirmed the generated functional groups on fiber surfaces during the oxidation treatment step. For un-oxidized CNFs, two characteristic peaks were indexed at 1280 cm<sup>−1</sup> and 1590 cm<sup>−1</sup>, which were attributed to the C–C and C=C stretch bonds, respectively. For oxidized CNFs, broad peaks at 3333 and 2957 cm<sup>−1</sup> were indexed for the −OH vibration of the −COOH group, and the intense peak at 1162 cm<sup>−1</sup> was attributed to the −C–O stretching of the −

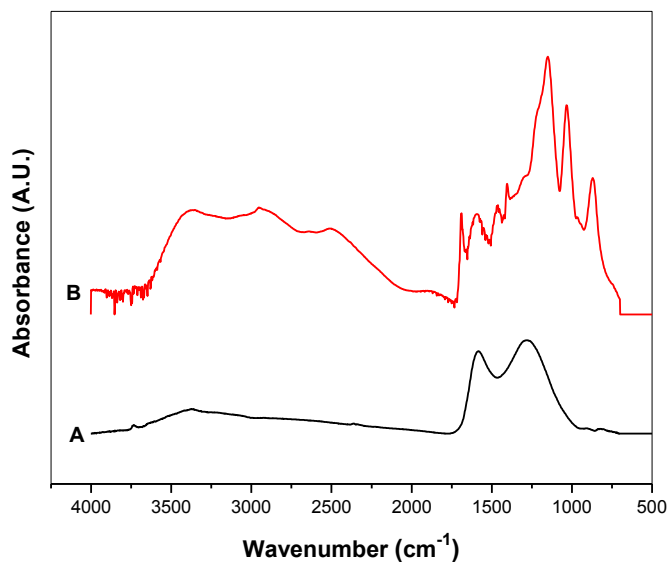


Fig. 2. FTIR spectra of (A) CNFs and (B) oxidized CNFs.

C–OH group. Oxidized CNFs also presented two characteristic bending mode peaks at  $1733\text{ cm}^{-1}$  and  $1690\text{ cm}^{-1}$ , respectively, corresponding to the  $\text{C}=\text{O}$  stretch bonds in esters and benzo-phenones [29].

The successful electrodeposition of  $\text{SnO}_2$  on the fiber surfaces was demonstrated by the energy-dispersive X-ray spectroscopy (EDS) analysis (Fig. 3). The EDS spectrum of PCNF@ $\text{SnO}_2$ @C composite clearly showed the existence of tin, oxygen, and carbon. The  $\text{SnO}_2$  contents in as-prepared nanofiber composites were investigated by the elemental analysis method and the results are shown in Table 1. The  $\text{SnO}_2$  content was calculated based on the contents of carbon, hydrogen, and nitrogen compositions in the  $\text{SnO}_2$ -containing CNF composites by assuming other impurities were negligible. It was seen that  $\text{SnO}_2$  contents were 35.7%, 24.1%, 40.8% and 38.5%, respectively, in CNF@ $\text{SnO}_2$ , CNF@ $\text{SnO}_2$ @C, PCNF@ $\text{SnO}_2$ , and PCNF@ $\text{SnO}_2$ @C composites. The  $\text{SnO}_2$  content in PCNF@ $\text{SnO}_2$  composite was higher than that of CNF@ $\text{SnO}_2$  composite, indicating that the increased surface area created by the porous structure in PCNFs is beneficial for the electrodeposition of  $\text{SnO}_2$  nanoparticles.

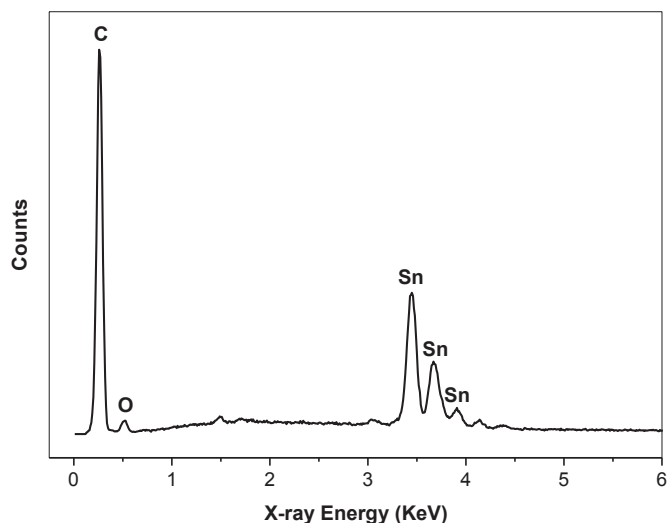


Fig. 3. EDS spectrum of PCNF@ $\text{SnO}_2$ @C composite.

Table 1

Compositions of nanofiber composites based on element analysis measurement.

Description of nanofiber composite	Compositions of nanofiber composites (wt%)	
	C	$\text{SnO}_2$
CNF@ $\text{SnO}_2$ composite	51.0	35.7
CNF@ $\text{SnO}_2$ @C composite	62.2	24.1
PCNF@ $\text{SnO}_2$ composite	47.6	40.8
PCNF@ $\text{SnO}_2$ @C composite	50.6	38.5

From Table 1, it was also seen that the carbon content increased after CVD carbon coating.

The morphology of CNF@ $\text{SnO}_2$ , CNF@ $\text{SnO}_2$ @C, PCNF@ $\text{SnO}_2$ , and PCNF@ $\text{SnO}_2$ @C composites was examined by using SEM (Fig. 4). From the SEM images, it was seen that the surface morphologies of all four nanofiber composites were similar.  $\text{SnO}_2$  was electrodeposited uniformly throughout the nanofiber surfaces without forming large aggregations. However, the porous structure and CVD carbon coating cannot be observed from the SEM images due to the limited resolution. Therefore, TEM characterization was employed to demonstrate the porous structure and thin CVD carbon coating as discussed below.

TEM images of CNFs, CNF@ $\text{SnO}_2$ , CNF@ $\text{SnO}_2$ @C, PCNFs, PCNF@ $\text{SnO}_2$ , and PCNF@ $\text{SnO}_2$ @C composites were presented in Fig. 5. Before electrodeposition, the surface of CNFs was smooth (Fig. 5A) and the porous structure created by the decomposition of PMMA was observable on PCNFs (Fig. 5D). However, as shown in Fig. 5B and E,  $\text{SnO}_2$  nanoclusters were formed along the nanofiber surfaces after the electrodeposition. The presence of  $\text{SnO}_2$  nanoclusters was more apparent in CVD carbon-coated nanofibers, i.e., CNF@ $\text{SnO}_2$ @C and PCNF@ $\text{SnO}_2$ @C composites (Fig. 5C and F). The CVD carbon coating layers were observable in higher-magnification TEM images, as shown in Fig. 6. It was seen that the thicknesses of the CVD carbon coating layers on CNF@ $\text{SnO}_2$ @C and PCNF@ $\text{SnO}_2$ @C composites were both around 10 nm. These nanoscale carbon coating layers are important for stable SEI formation on the surfaces of active materials during the repetitive electrochemical reactions.

Fig. 7 shows X-ray diffraction (XRD) patterns of CNFs, CNF@ $\text{SnO}_2$ , and CNF@ $\text{SnO}_2$ @C composites. For comparison, the XRD pattern of un-calcined CNF@ $\text{SnO}_2$  composite is also shown. Un-calcined CNF@ $\text{SnO}_2$  composite exhibited diffraction peaks at  $2\theta$  of about  $27^\circ$ ,  $34^\circ$ , and  $52^\circ$ , which represented the (110), (101), and (211) planes of the  $\text{SnO}_2$  phase (JCPDS No. 41-1445), respectively. The intensities of these indexed peaks were relatively low, indicating the small sizes of tetragonal  $\text{SnO}_2$  nanocrystals [12,30]. After calcination, similar peaks were observable for CNF@ $\text{SnO}_2$  composite, but peak intensities decreased significantly.  $\text{SnO}_2$  peak intensities of CNF@ $\text{SnO}_2$ @C composite were further weakened with the introduction of CVD amorphous carbon coating. In addition, as shown in Fig. 7, all four nanofiber composites showed a broad and weak diffraction peak at around  $2\theta = 25^\circ$ , which could be indexed as the (002) planes of disordered carbon structure. This indicates the amorphous nature of both the carbon nanofiber matrix and CVD carbon coating [31].

### 3.2. Electrochemical performance

In order to evaluate the electrochemical performance of the as-prepared nanofiber composites for use as anodes in lithium-ion batteries, galvanostatic charge–discharge tests were conducted between 0.01 and 2.0 V at a constant current density of  $100\text{ mA g}^{-1}$ . Fig. 8 shows the galvanostatic charge–discharge profiles for the



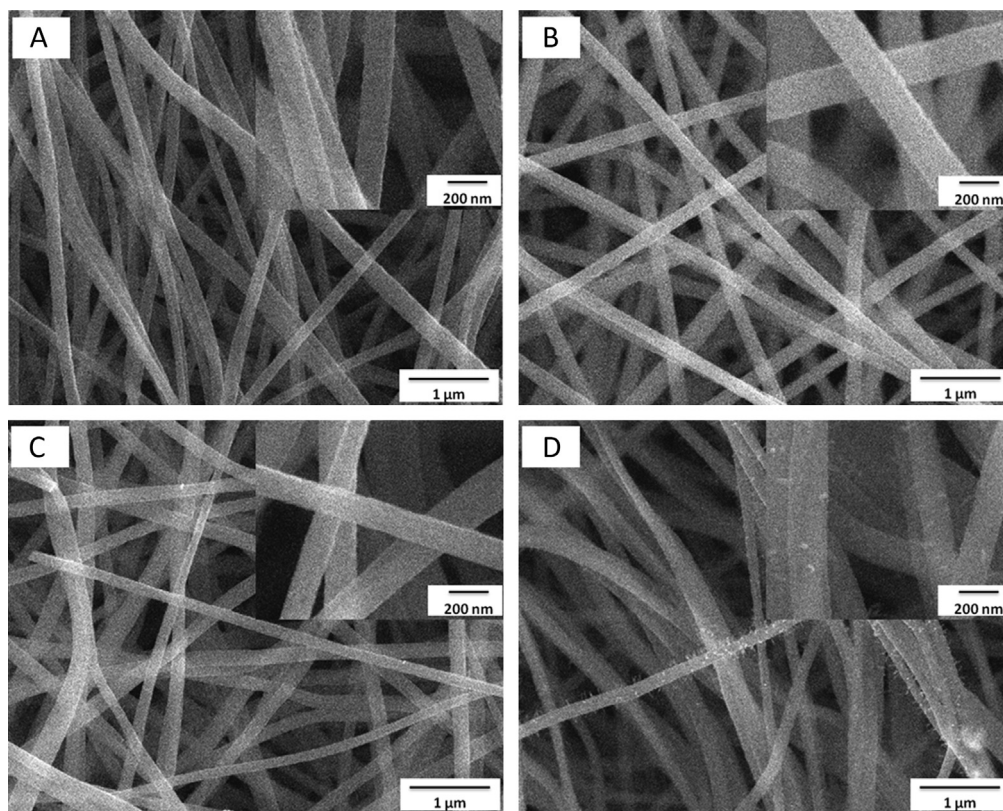


Fig. 4. SEM images of (A) CNF@SnO<sub>2</sub>, (B) CNF@SnO<sub>2</sub>@C, (C) PCNF@SnO<sub>2</sub>, and (D) PCNF@SnO<sub>2</sub>@C composites.

first, second and fifth cycles of CNF@SnO<sub>2</sub>, CNF@SnO<sub>2</sub>@C, PCNF@SnO<sub>2</sub>, and PCNF@SnO<sub>2</sub>@C composites. At the first cycle, the charge capacities were 1167, 1176, 1315, and 1157 mAh g<sup>-1</sup>, respectively, for CNF@SnO<sub>2</sub>, CNF@SnO<sub>2</sub>@C, PCNF@SnO<sub>2</sub>, and PCNF@SnO<sub>2</sub>@C composites. The intention of using PCNF structure was to increase the total surface area and hence the electrodeposition amount of active SnO<sub>2</sub> material. The element analysis has demonstrated that the SnO<sub>2</sub> content in PCNF@SnO<sub>2</sub> composite was higher than that in CNF@SnO<sub>2</sub> composite (Table 1), which was the main reason for PCNF@SnO<sub>2</sub> composite to have larger capacity than CNF@SnO<sub>2</sub> composite in the first cycle. From Fig. 8, it was also seen the CVD carbon coating reduced the first-cycle charge capacity of PCNF@SnO<sub>2</sub>@C composite. For all samples, a plateau identified at around 0.8 V at the first charge curve was attributed to the reduction of SnO<sub>2</sub> to Sn and Li<sub>2</sub>O, the decomposition of electrolyte, and the formation of solid electrolyte interface (SEI) layer on the active material surface [32,33]. In addition, this voltage plateau was extended after CVD carbon coating. Despite the different voltage plateaus of CVD carbon-coated and un-coated nanofiber composites, first-cycle coulombic efficiency values were very similar, i.e., 65.2%, 64.8%, 64.1%, and 64.7% for CNF@SnO<sub>2</sub>, CNF@SnO<sub>2</sub>@C, PCNF@SnO<sub>2</sub>, and PCNF@SnO<sub>2</sub>@C composites, respectively. The coulombic efficiencies increased to 94.9%, 95.9%, 94.7%, and 97.5%, respectively, at the second cycle for CNF@SnO<sub>2</sub>, CNF@SnO<sub>2</sub>@C, PCNF@SnO<sub>2</sub>, and PCNF@SnO<sub>2</sub>@C composites. The coulombic efficiencies of these four nanofiber composites further increased to 98.1%, 98.4%, 98.0%, and 99.1%, respectively, at the fifth cycle. Both at the second and fifth cycles, the coulombic efficiencies of CNF@SnO<sub>2</sub>@C and PCNF@SnO<sub>2</sub>@C composites were higher than those of CNF@SnO<sub>2</sub> and PCNF@SnO<sub>2</sub> composites.

The cycling performance of CNF@SnO<sub>2</sub> and CNF@SnO<sub>2</sub>@C composites was evaluated at a constant current density of 100 mA g<sup>-1</sup> (Fig. 9). For comparison, the cycling performance of electrospun

CNFs is also shown. It was seen that at the 100th cycle, the capacity of electrospun CNFs was around 269 mAh g<sup>-1</sup> and the corresponding capacity retention was 55.40%. For CNF@SnO<sub>2</sub> composite, the capacity at the 100th cycle was around 469 mAh g<sup>-1</sup>, which corresponded to increased capacity retention of 61.67%. Based on the CNF@SnO<sub>2</sub> composite composition, the capacity residing with the Sn component at the twentieth cycle was calculated to be 858.9 mAh g<sup>-1</sup>, which is close to theoretical lithium storage capacity (991 mAh g<sup>-1</sup>) of pure Sn [10]. The cycling performance was further improved by the introduction of CVD carbon coating. The capacity of CNF@SnO<sub>2</sub>@C composite at the 100th cycle was around 528 mAh g<sup>-1</sup> and the corresponding capacity retention was increased to 69.23%. CNF@SnO<sub>2</sub>@C composite also exhibited a high coulombic efficiency of 99.6% at the 100th cycle. This result demonstrated that the nanoscale carbon coating layer supported more stable SEI formation by preventing direct contact of the electrolyte with the active SnO<sub>2</sub> material. Similar effects of nanoscale carbon coating have been observed by Nam et al., who obtained improved cycling stability for nanoscale carbon-coated spherical SnO<sub>2</sub> nanoparticle anodes [34]. Chen et al. also demonstrated stable SEI formation on SnO<sub>2</sub> spheres by suitable carbon coating [35].

The cycling performance comparison of PCNFs, PCNF@SnO<sub>2</sub> and PCNF@SnO<sub>2</sub>@C composites is demonstrated in Fig. 10. The capacity of PCNFs, PCNF@SnO<sub>2</sub> and PCNF@SnO<sub>2</sub>@C composites at the 100th cycle was 263, 554, and 586 mAh g<sup>-1</sup>, respectively. Corresponding capacity retentions were 54.90%, 65.67%, and 78.30%, respectively, at the 100th cycle. Therefore, the cycling performance of PCNF@SnO<sub>2</sub> composite was also improved by CVD carbon coating. For the PCNF@SnO<sub>2</sub> composite, the capacity provided by the Sn component at the twentieth cycle was calculated to be 973.5 mAh g<sup>-1</sup>, which is close to theoretical capacity of Sn. Comparing Figs. 8 and 9, it was seen that the capacity of

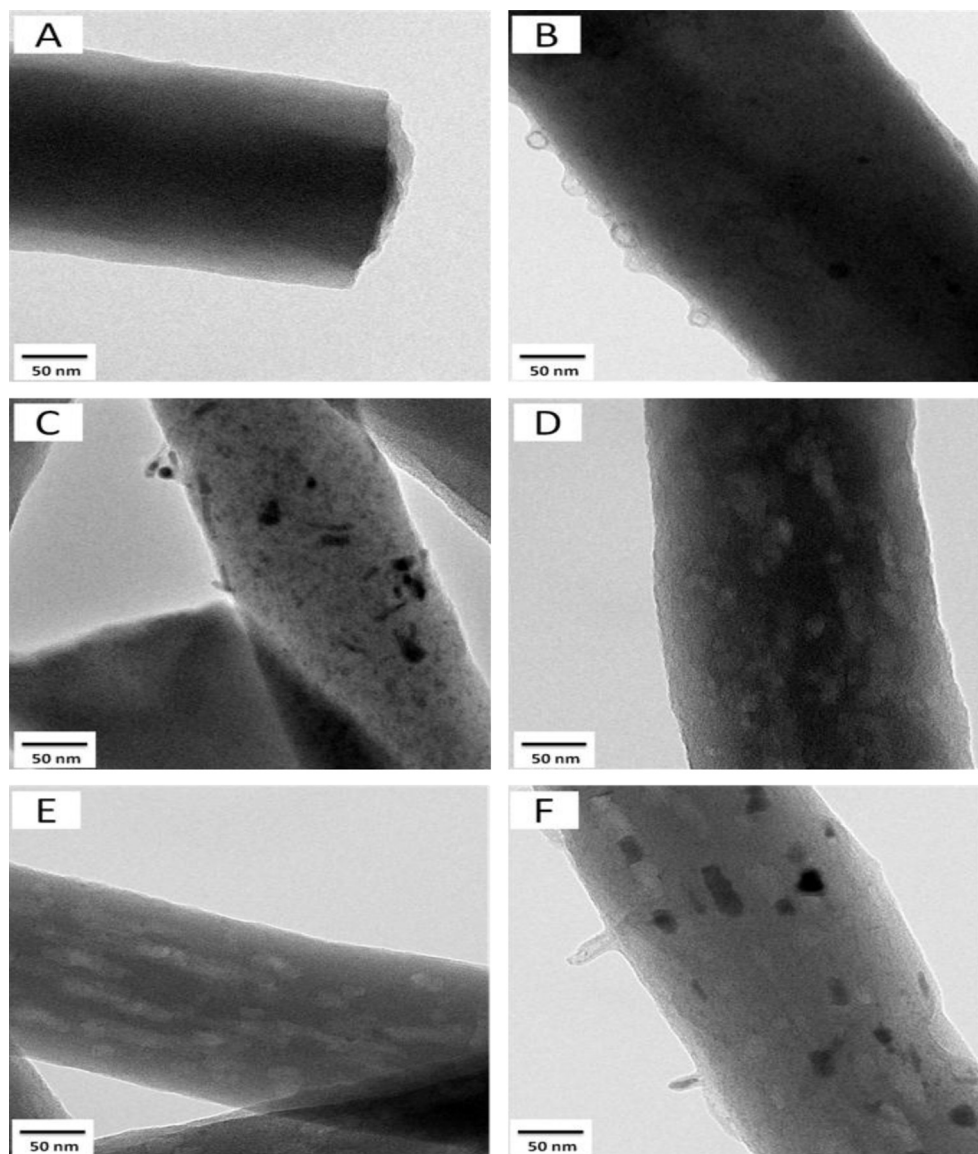


**Fig. 5.** TEM images of (A) CNFs, (B) CNF@SnO<sub>2</sub>, (C) CNF@SnO<sub>2</sub>@C, (D) PCNFs, (E) PCNF@SnO<sub>2</sub>, and (F) PCNF@SnO<sub>2</sub>@C composites.

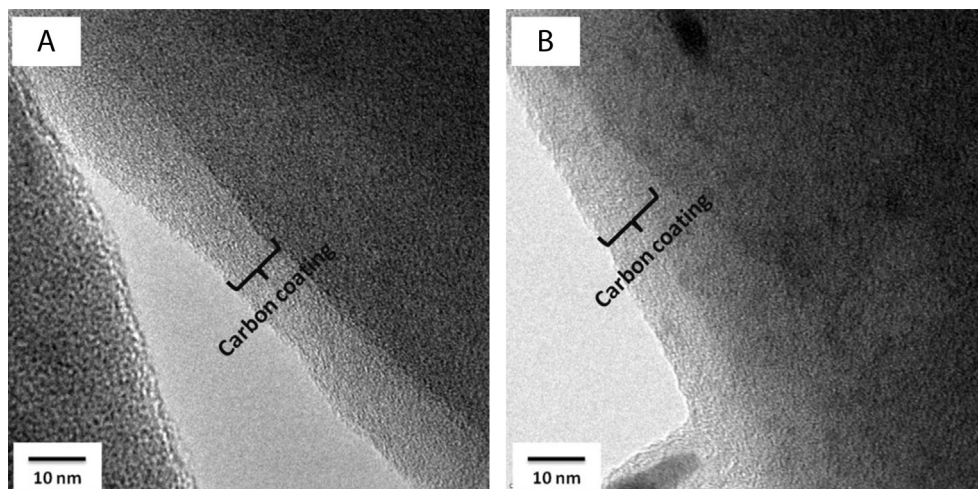


**Fig. 6.** High-magnification TEM images of (A) CNF@SnO<sub>2</sub>@C and (B) PCNF@SnO<sub>2</sub>@C composites.

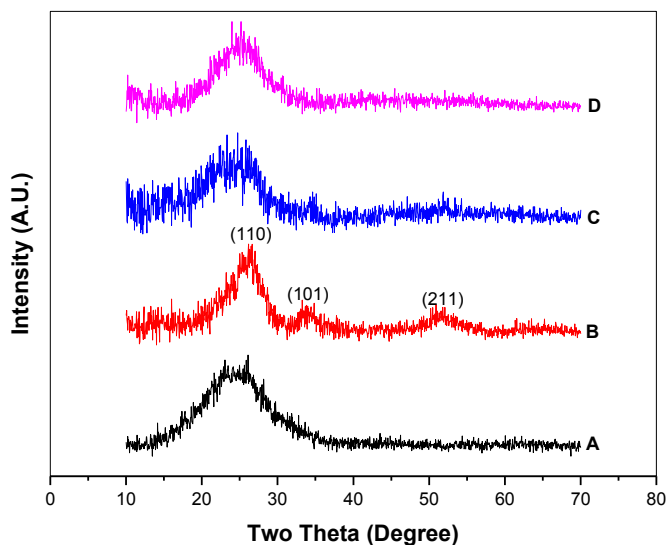


Fig. 7. WAXD patterns of (A) CNFs, (B) CNF@SnO<sub>2</sub> (un-calcined), (C) CNF@SnO<sub>2</sub>, and (D) CNF@SnO<sub>2</sub>@C composites.

PCNF@SnO<sub>2</sub>@C composite (586 mAh g<sup>-1</sup>) was higher than that of CNF@SnO<sub>2</sub>@C composite (528 mAh g<sup>-1</sup>) at the 100th cycle. This is probably because of the high SnO<sub>2</sub> content in PCNF@SnO<sub>2</sub>@C composite (see Table 1). Among all four different nanofiber composites studied, the highest capacity and capacity retention were achieved by PCNF@SnO<sub>2</sub>@C composite. Compared to solid CNFs, porous CNFs could allow more SnO<sub>2</sub> to be deposited on the surface during electrodeposition, leading to higher capacity. In addition, both the porous structure and CVD carbon coating help accommodate the volume change of SnO<sub>2</sub> particles, thereby resulting in

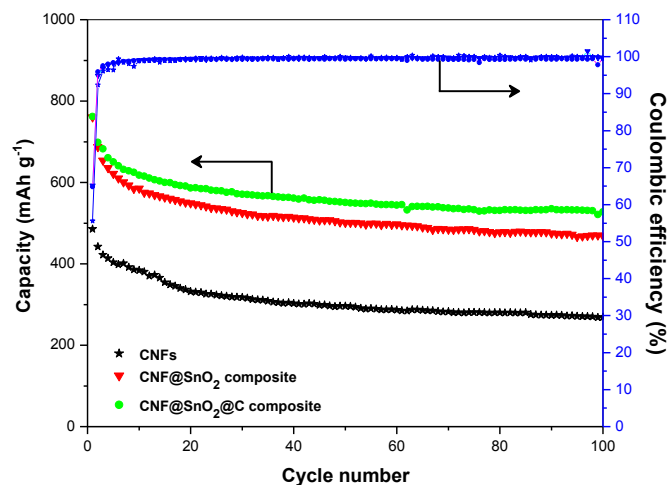


Fig. 9. Cycling performance comparison of CNFs, CNF@SnO<sub>2</sub>, and CNF@SnO<sub>2</sub>@C composites.

improved cycling performance. The CVD carbon coating can also stabilize the SEI formation on the surface, which is beneficial in increasing the coulombic efficiency. Similar design has been used by Wu et al., who prepared CNT@SnO<sub>2</sub>@C coaxial nanocables with different carbon thicknesses to improve the cycling performance of CNT@SnO<sub>2</sub> anodes [19]. Their results demonstrated that without the porous structure, the capacity of CNT@SnO<sub>2</sub>@C coaxial nanocables decreased to less than 600 mAh g<sup>-1</sup> after 10 cycles even with a thick carbon coating of 10 nm.

The rate capability of PCNF@SnO<sub>2</sub>@C composite, which showed the best cycling performance among all studied nanofiber composites, was investigated under different current densities (Fig. 11).

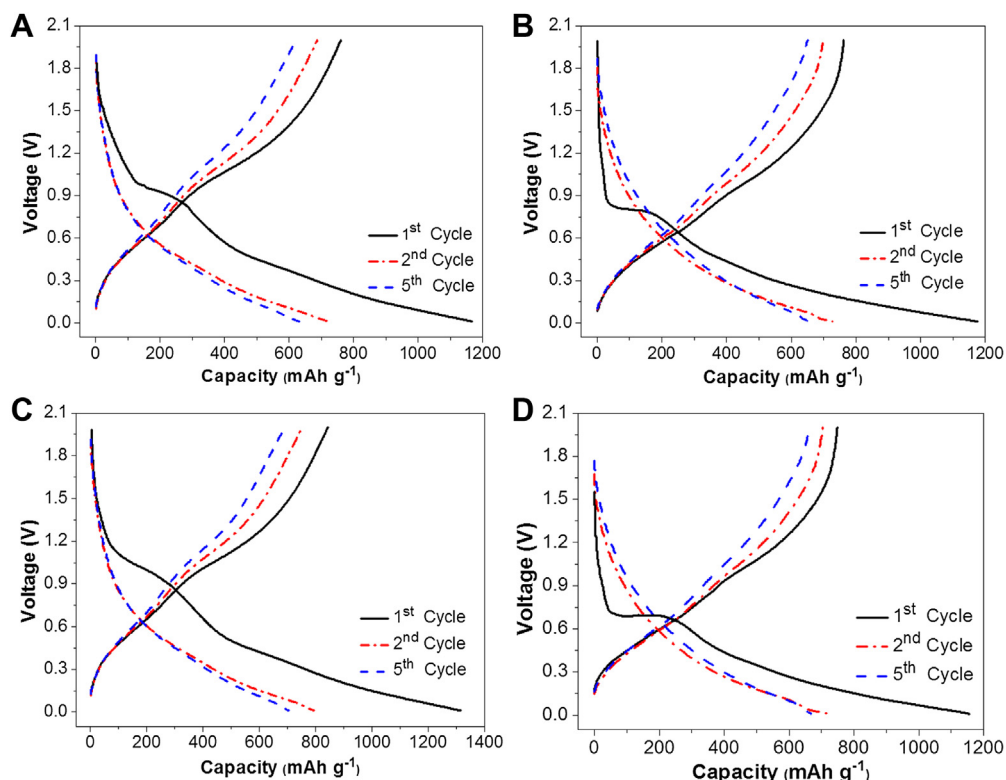


Fig. 8. Galvanostatic charge–discharge profiles of (A) CNF@SnO<sub>2</sub>, (B) CNF@SnO<sub>2</sub>@C, (C) PCNF@SnO<sub>2</sub>, and (D) PCNF@SnO<sub>2</sub>@C composites.



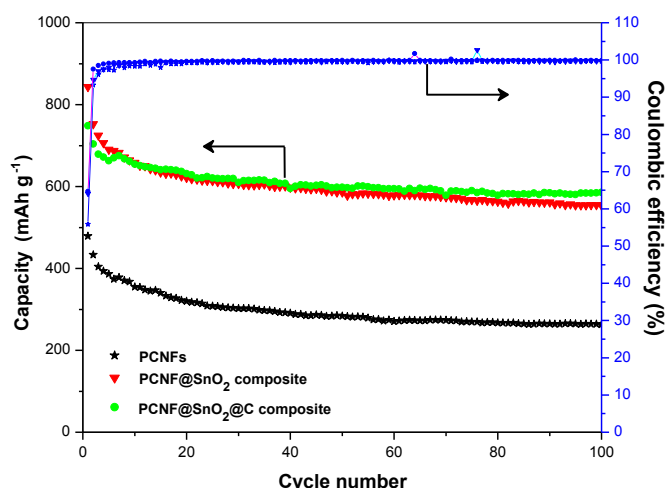


Fig. 10. Cycling performance comparison of PCNFs, PCNF@SnO<sub>2</sub>, and PCNF@SnO<sub>2</sub>@C composites.

The average charge capacity values of PCNF@SnO<sub>2</sub>@C composite were around 713, 568, 463, and 398 mAh g<sup>-1</sup>, respectively, at 100, 200, 400, and 800 mA g<sup>-1</sup>. The coulombic efficiency did not show apparent change as the current density increased and it was still more than 99% even at the highest current density of 800 mA g<sup>-1</sup>. The charge capacity value returned to 600 mAh g<sup>-1</sup> under a reduced current density of 100 mA g<sup>-1</sup> after undergoing cycles at higher current densities. This charge capacity (600 mAh g<sup>-1</sup>) was similar to the initial charge capacities, which also demonstrated the good rate capability of PCNF@SnO<sub>2</sub>@C composite.

#### 4. Conclusions

CNF@SnO<sub>2</sub> and PCNF@SnO<sub>2</sub> composites were developed as binder-free anodes for lithium-ion batteries by the electrodeposition of SnO<sub>2</sub> nanoparticles on electrospun carbon nanofibers. To achieve improved cycling performance, additional CVD amorphous carbon coating was also applied to form CNF@SnO<sub>2</sub>@C and PCNF@SnO<sub>2</sub>@C composites. It was found that the amount of electrodeposited SnO<sub>2</sub> nanoparticles and corresponding capacity value increased by using the PCNF structure. The capacity of PCNF@SnO<sub>2</sub>@C composite was measured to be 554 mAh g<sup>-1</sup> at the 100th cycle,

which was higher than that (469 mAh g<sup>-1</sup>) for CNF@SnO<sub>2</sub> composite. In addition, the long-term cycling performance of both CNF@SnO<sub>2</sub> and PCNF@SnO<sub>2</sub> composites was improved with nano-scale CVD carbon coating on the fiber surfaces. At the 100 cycle, the capacity retentions of the resultant CNF@SnO<sub>2</sub>@C and PCNF@SnO<sub>2</sub>@C composites were 69.23% and 78.30%, respectively. It was, therefore, demonstrated that among all nanofiber composites studied, PCNF@SnO<sub>2</sub>@C composite is the most promising anode material candidate with the largest capacity and best cycling performance.

#### Acknowledgments

This research was supported by Advanced Transportation Energy Center and ERC Program of the National Science Foundation under Award Number EEC-08212121. The authors thank Dr. Philip D. Bradford and Ozkan Yildiz for use of the chemical vapor deposition furnace.

#### References

- [1] X. Zhang, L. Ji, O. Toprakci, Y. Liang, M. Alcoutlabi, *Polym. Rev.* 51 (2011) 239–264.
- [2] X. Yu, S. Yang, B. Zhang, D. Shao, X. Dong, Y. Fang, Z. Li, H. Wang, *J. Mater. Chem.* 21 (2011) 12295–12302.
- [3] X. Liu, M. Wu, M. Li, X. Pan, J. Chen, X. Bao, *J. Mater. Chem. A* 1 (2013) 9527–9535.
- [4] L. Zhang, G. Zhang, H.B. Wu, L. Yu, X.W.D. Lou, *Adv. Mater.* 25 (2013) 2589–2593.
- [5] K. Fu, O. Yildiz, H. Bhanushali, Y. Wang, K. Stano, L. Xue, X. Zhang, P.D. Bradford, *Adv. Mater.* 25 (2013) 5109–5114.
- [6] S. Zhang, Y. Li, G. Xu, S. Li, Y. Lu, O. Toprakci, X. Zhang, *J. Power Sources* 213 (2012) 10–15.
- [7] H. Wu, G. Zheng, N. Liu, T.J. Carney, Y. Yang, Y. Cui, *Nano Lett.* 12 (2012) 904–909.
- [8] B.-S. Lee, S.-B. Son, K.-M. Park, J.-H. Seo, S.-H. Lee, I.-S. Choi, K.-H. Oh, W.-R. Yu, *J. Power Sources* 206 (2012) 267–273.
- [9] F. Han, W.-C. Li, M.-R. Li, A.-H. Lu, *J. Mater. Chem.* 22 (2012) 9645–9651.
- [10] X. Guo, X. Fang, Y. Sun, L. Shen, Z. Wang, L. Chen, *J. Power Sources* 226 (2012) 75–81.
- [11] X.W. Lou, C.M. Li, L.A. Archer, *Adv. Mater.* 21 (2009) 2536–2539.
- [12] J.S. Chen, Y.L. Cheah, Y.T. Chen, N. Jayaprakash, S. Madhavi, Y.H. Yang, X.W. Lou, *J. Phys. Chem. C* 113 (2009) 20504–20508.
- [13] H.X. Zhang, C. Feng, Y.C. Zhai, K.L. Jiang, Q.Q. Li, S.S. Fan, *Adv. Mater.* 21 (2009) 2299–2304.
- [14] X. Sun, J. Liu, Y. Li, *Chem. Mater.* 18 (2006) 3486–3494.
- [15] X. Huang, X. Zhou, L. Zhou, K. Qian, Y. Wang, Z. Liu, C. Yu, *ChemPhysChem* 12 (2011) 278–281.
- [16] Y. Li, S. Zhu, Q. Liu, J. Gu, Z. Guo, Z. Chen, C. Feng, D. Zhang, W.-J. Moon, *J. Mater. Chem.* 22 (2012) 2766–2773.
- [17] J. Kong, Z. Liu, Z. Yang, H.R. Tan, S. Xiong, S.Y. Wong, X. Li, X. Lu, *Nanoscale* 4 (2012) 525–530.
- [18] M. He, L. Yuan, X. Hu, W. Zhang, J. Shu, Y. Huang, *Nanoscale* 5 (2013) 3298–3305.
- [19] P. Wu, N. Du, H. Zhang, J. Yu, D. Yang, *J. Phys. Chem. C* 114 (2010) 22535–22538.
- [20] X.-Y. Fan, X.-Y. Shi, J. Wang, Y.-X. Shi, J.-J. Wang, L. Xu, L. Gou, D.-L. Li, *J. Solid State Electrochem.* 17 (2013) 201–208.
- [21] C.A. Bonino, L. Ji, Z. Lin, O. Toprakci, X. Zhang, S.A. Khan, *ACS Appl. Mater. Interfaces* 3 (2011) 2534–2542.
- [22] S. Ding, J.S. Chen, X.W. Lou, *Chem. Asian J.* 6 (2011) 2278–2281.
- [23] J. Liu, W. Li, A. Manthiram, *Chem. Commun.* 46 (2010) 1437–1439.
- [24] X.W. Lou, D. Deng, J.Y. Lee, L.A. Archer, *Chem. Mater.* 20 (2008) 6562–6566.
- [25] L. Ji, Z. Lin, B. Guo, A.J. Medford, X. Zhang, *Chem. Eur. J.* 16 (2010) 11543–11548.
- [26] Z. Lin, L. Ji, M.D. Woodroof, X. Zhang, *J. Power Sources* 195 (2010) 5025–5031.
- [27] M.-S. Wu, Y.-H. Ou, Y.-P. Lin, *Electrochim. Acta* 55 (2010) 3240–3244.
- [28] A. Rasheed, J.Y. Howe, M.D. Dadmun, P.F. Britt, *Carbon* 45 (2007) 1072–1080.
- [29] Z. Lin, L. Ji, X. Zhang, *Mater. Lett.* 63 (2009) 2115–2118.
- [30] Y. Li, X. Lv, J. Lu, J. Li, *J. Phys. Chem. C* 114 (2010) 21770–21774.
- [31] K. Fu, L. Xue, O. Yildiz, S. Li, H. Lee, Y. Li, G. Xu, L. Zhou, P.D. Bradford, X. Zhang, *Nano Energy* 2 (2013) 976–986.
- [32] R. Yang, W. Zhao, J. Zheng, X. Zhang, X. Li, *J. Phys. Chem. C* 114 (2010) 20272–20276.
- [33] S. Ding, D. Zhang, H.B. Wu, Z. Zhang, X.W.D. Lou, *Nanoscale* 4 (2012) 3651–3654.
- [34] S. Nam, S. Kim, S. Wi, H. Choi, S. Byun, S.-M. Choi, S.-I. Yoo, K.T. Lee, B. Park, *J. Power Sources* 211 (2012) 154–160.
- [35] L. Chen, X. Yin, L. Mei, C. Li, D. Lei, M. Zhang, Q. Li, Z. Xu, C. Xu, T. Wang, *Nanotechnology* 23 (2012) 035402.

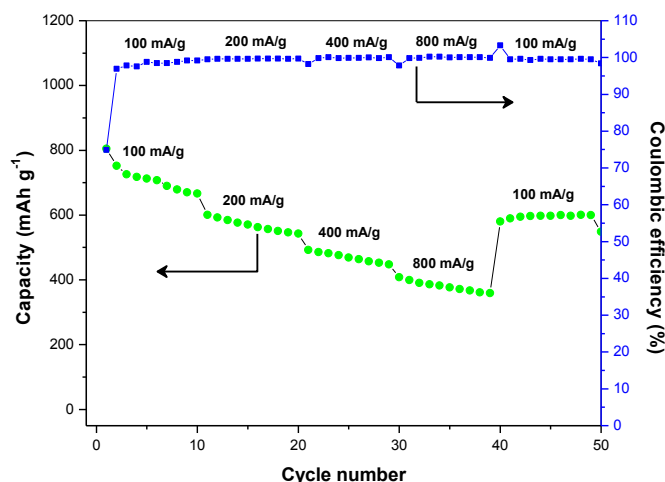


Fig. 11. Rate capability of PCNF@SnO<sub>2</sub>@C composite cycled at different current densities.